RSC Advances

PAPER

View Article Online
View Journal | View Issue

Cite this: *RSC Adv.*, 2025, **15**, 24223

Impacts of r-GO and N-doping on the structural, magnetic, optical and photocatalytic properties of $CuAl_2O_4$: enhanced crystal violet removal under solar light irradiation

Dilshad Ahmad,[a] Ismat Bibi,*[a] Farzana Majid,[b] Shagufta Kamal,[c] Sooman Lim,[d] Norah Alwadai,[e] Qasim Raza,[a] Muhammad Aamir,[f] Arif Nazir[g] and Munawar Iqbal*[h]

Designing a magnetically recyclable and visible-light-driven photocatalyst is of great importance in environmental remediation. Realizing efficient removal of persistent azo dyes from industrial wastewater is still a major challenge for researchers. In this context, herein, novel $CuAl_2O_4$ and N/rGO nanohybrids, CA-N/GO(1–4), were synthesized *via* an ultrasonic method and assessed for their efficiency toward the photocatalytic removal of crystal violet (CV) dye from simulated polluted water under visible irradiation. Crystalline phase, morphology and functional groups of the synthesized materials were examined using XRD, SEM and FTIR spectroscopy, respectively, while their magnetic and optical behaviors were tested using VSM, PL and UV-visible spectroscopic techniques. XRD results showed that the cubic spinel phase of pure $CuAl_2O_4$ (CAO) exhibited a 57.32 nm mean crystallite size that was altered upon substitution of N/rGO in the composites. SEM images revealed the successful incorporation of CAO nanoparticles in N/rGO sheets. $CuAl_2O_4$-N/rGO4 (CA-N/GO4) catalyst exhibited excellent catalytic efficiency (*i.e.*, 82.6% removal of dye in 90 min), which was significantly higher than those of pure CAO and N/rGO. After optimizing the reaction conditions, almost complete removal of dye was achieved for 30 mg L^{-1} of catalyst dosage at pH = ~10. This robust photocatalytic performance might be attributed to N/rGO, which hindered the recombination of electron–hole pairs, thus enhancing the surface area and providing more active sites for dye adsorption. A possible mechanism of CV degradation was proposed using different scavenging agents. Structural stability and practical utility of the used CA-N/GO4 catalyst were assessed after four continuous runs, which demonstrated good outcomes. Thus, these results reveal that the novel and magnetically separable CA-N/GO4 nanohybrid has a remarkable prospect for the elimination of toxic dyes from industrial sewage water under visible irradiation.

Received 3rd April 2025
Accepted 25th June 2025

DOI: 10.1039/d5ra02304a

rsc.li/rsc-advances

1. Introduction

In recent decades, the increasing demands for industrial wastewater treatment, environmental remediation and renewable energy sources have been discussed as hot issues. Among these, water pollution is a major global challenge that increases day by day, which needs to be resolved with appropriate and efficient methods.[1,2] The largest contributors of water pollution include textile, tanning, printing, and dying industries and other units that discharge significant amounts of aromatic-based organic dyes into running water bodies. Such industrial pollutants are hazardous and toxic to marine life and human beings.[3] Thus, for a healthy life, it is necessary to filter and clean the industrial wastewater to shield the water bodies from these pollutants. In this regard, numerous physical, chemical and biological techniques, such as adsorption, chemical oxidation, coagulation, microbial treatment, the Fenton process, filtration, advanced oxidation processes (AOPs) and ultrasound-mediated processes, have been extensively utilized to remove these toxic dyes from industrial wastewater.[4,5] However, these strategies are less efficient and have limitations, such as poor dye degradation and high consumption of energy. Hence novel, cost-effective and eco-friendly routes are needed for the complete removal

[a]*Institute of Chemistry, The Islamia University of Bahawalpur, Bahawalpur, Pakistan. E-mail: drismat@iub.edu.pk*

[b]*Department of Physics, University of the Punjab, Lahore, Pakistan*

[c]*Department of Biochemistry, Government College University, Faisalabad 38000, Pakistan*

[d]*Graduate School of Flexible and Printable Electronics, LANL-JBNU Engineering Institute-Korea, Jeonbuk National University, Jeonju, 54896, Republic of Korea*

[e]*Department of Physics, College of Sciences, Princess Nourah bint Abdulrahman University, P. O. Box 84428, Riyadh 11671, Saudi Arabia*

[f]*Department of Chemistry, University of Layyah, Layyah, Pakistan*

[g]*Department of Chemistry, The University of Lahore, Lahore, Pakistan*

[h]*School of Chemistry, University of the Punjab, Lahore, Pakistan. E-mail: bosalvee@yahoo.com*

of organic dyes from industrial effluents.[6,7] Photocatalysis is regarded as a convenient route for hydrogen generation, ammonia production, disinfection and removal of organic dyes owing to its efficient properties, such as non-toxicity, high efficiency and cost effectiveness.[8,9]

Semiconductor-based photocatalysis holds wide promise as an economic and feasible pathway for hydrogen production, air purification and pollutant degradation from industrial wastewater.[10–12] In recent years, SnO_2, TiO_2,[13] PbO_2, MnO_2, WO_3, and BiOCl,[14] as semiconductor photocatalysts, have been utilized widely in the degradation of organic dyes owing to their robust redox ability and excellent structural stability. However, some serious drawbacks such as their wide optical bandgap and low sensitivity in the UV region of the solar spectrum limit their practical utility.[15,16] Hence, the development of novel materials with narrow bandgaps and visible-light-active photocatalytic constituents is widely pursued.[17–20]

Recently, spinel-type semiconducting aluminates, such as $CuAl_2O_4$, $ZnAl_2O_4$, $NiAl_2O_4$, $MgAl_2O_4$, and $LiAl_2O_4$, have gained much attention of researchers in the removal of industrial dyes owing to their good photocatalytic and magnetic properties.[21] Among these, copper aluminate ($CuAl_2O_4$) is a p-type semiconductor with unique properties such as high thermal stability and mechanical resistance, hydrophobicity, low cost, nontoxicity, corrosive resistance, low surface acidity and high catalytic activity.[22] With a tuned band gap in the range of 1.8–2.3 eV, visible light absorption, and high photochemical stability, it has attracted remarkable attention for photocatalytic treatment.[23] Zhang *et al.* fabricated CAO nanofibers that exhibited good catalytic activity towards the elimination of rhodamine B and methyl orange dyes using an electrospinning/annealing strategy.[24] The CAO photocatalyst was synthesized *via* sonication and used for the mineralization of methyl orange under visible light irradiation.[25] Being a soft ferromagnetic material, it agglomerates owing to magnetic interactions that result in a decrease in active sites, which is necessary for the degradation process.[26] However, its narrow bandgap limits its widespread applications in photocatalysis owing to the fast recombination of photo-induced charge carriers on its surface. Hence, a possible solution to this challenge might be the construction of a heterojunction, particularly a p–n junction, which may easily build an electric field internally to assist the charge transfer and separation of charge carriers at the interface.[27]

To overcome the agglomeration and fast recombination of charge carriers, surface alteration of CAO carbon-based planner sheets, such as reduced graphene, has been proven as a promising strategy for improved photocatalytic degradation of dyes.[28] Reduced graphene oxide (rGO) is a two-dimensional sp^2 hybridized carbon material, which possess a high surface area, good structural stability and excellent electrical conductivity.[26] Graphene has been widely used as a supportive material in its composite form with other metal oxides and sulphides for the photodegradation of azo dyes. Metal (Zn or Y) or non-metal doping (N, P, S, or B) in rGO, resulting in the generation of structural defects and availability of charge carriers on it, is a promising strategy to enhance its catalytic activity.[28] Nitrogen doping in rGO sheets can enhance their chemical reactivity by introducing certain structural defects and active sites. Discharged effluents such as dyes, heavy metals and pharmaceutical residues have significant interactions with these active sites. Additionally, this doping facilitates the delocalization of π-electrons in the graphene structure, which increases the electron transport rate that is necessary for the degradation by photocatalysis. Even in challenging wastewater conditions, N-doped rGO exhibits superior chemical and thermal stabilities. Furthermore, it maintains its efficacy during several treatment cycles, which increases its cost-effectiveness for everyday use.[6,28] Nitrogen-doped rGO in its composite form has been reported by various researchers, *i.e.*, a $NiAl_2O_4$@N-rGO heterojunction was prepared for the photocatalytic degradation of crystal violet dye under visible light irradiation.[29] Chnadel *et al.* reported AgBr/Zn(Co)Fe_2O_4/N-rGO for efficient removal of malachite green and methyl orange dyes.[30] Similarly, N-rGO/S-gC_3N_4 nanohybrids were fabricated and used effectively for the removal of 4-nitrophenol.[31] Based on these works, we have fabricated a series of pure CAO, N/rGO and CA-N/GO(1–4) heterojunctions with different weight ratios by considering the valence and conduction band potentials of CAO and N/rGO. This type of heterojunction for the photo removal of CV dye under visible light irradiation has not been reported yet. The as-synthesized nanocomposites were characterized for their structural, morphological, optical and photocatalytic behavior using powder XRD and photoluminescence (PL) techniques. These novel nanohybrids were assessed for their responsive photo removal of CV dye under visible irradiation. Furthermore, the probable mechanism for photocatalytic activity of CA-N/GO4 and the operational parameters (*i.e.*, initial pH of the reaction mixture, catalyst dose and concentration of the dye) that affect the degradation of dye were discussed comprehensively.

2. Materials and synthesis procedure

2.1. Materials and reagents

The chemical precursors used for the synthesis of $CuAl_2O_4$ were copper nitrate trihydrate (99%), aluminum nitrate nonahydrate (99.9%), aqueous ammonia (32%) and double distilled water (DDW). Meanwhile, the preparation of N/rGO used ammonia solution (25%), ammonium nitrate, graphite flake powder (98 wt%), H_2SO_4 (98%), $KMnO_4$, H_2O_2 (30%), conc. HCl and hydrazine. All the chemicals were acquired from Sigma Aldrich purity and were used without additional purification.

2.2. Synthesis of $CuAl_2O_4$ NPs

In this work, pure $CuAl_2O_4$ NPs were prepared *via* a co-precipitation method of metal ions, as reported in a previous study.[32] Following the synthesis protocol, aqueous solutions of 1 M Cu and 2 M Al nitrate were prepared and mixed. The resulting mixture was magnetically stirred for half an hour, followed by heating up to 60 °C for homogeneous mixing of both the solutions. Then, aqueous ammonia, as the precipitation agent, was added dropwise to this mixture (until pH ~10 was reached) to carry out the simultaneous precipitation of Al and Cu in their hydroxide forms. A light blue precipitated

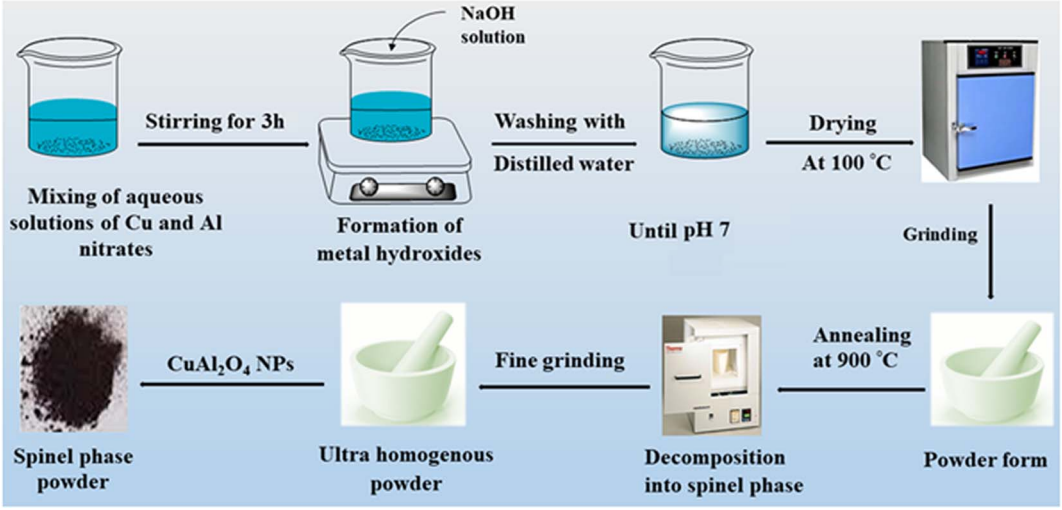

Fig. 1 Schematic of the synthesis of pure CAO nanoparticles *via* the co-precipitation method.

material was observed that was washed several times with DDS until pH 7 was attained, to minimize its basic character. This neutralized slurry was subjected to heating in an electric oven for drying at 100 °C, where almost all the moisture content was removed. Finally, the dried material was calcined for 6 h at 900 °C (Fig. 1).

2.3. Synthesis of graphene oxide (GO)

Graphene oxide (GO) was synthesized by a modified Hummers' method as reported in our previous study.[32] For synthesis, 3.0 g of each of the graphite powder and $NaNO_3$ was taken in a 2000 mL beaker. Then, 150 mL of conc. H_2SO_4 was added under constant stirring, where a dark-colored mixture was obtained. Later on, about 18 g of $KMnO_4$ was steadily added, followed by mixing (about 1 h) in an ice bath, which turned the mixture's color from dark black to greenish. The ice bath was removed while the stirring was continued for 48 hours at room temperature, with a thick paste (brown-slurry color) appearing upon adding 200 mL of de-ionized (DI) water to it. To this slurry, 500 mL of warm water was added along with the slow addition of 60 mL of H_2O_2 (reducing agent) that turned it into a thick yellowish suspension. This suspension was washed three times: first with H_2O_2 (1%), then H_2SO_4 (6%) and finally with DI water until pH 7 was reached and a dark brownish color graphene oxide (GO) paste was obtained.

2.4. Synthesis of CA-N/GO(1–4) nanocomposites

The as-synthesized GO was reduced into N/rGO as follows: 30 mL of GO suspension was taken, in which 450 mL of DDW was added to homogenize it *via* ultra-sonication at 300 K for 1 hour to achieve a homogenous blend of GO sheets. To this GO suspension, 0.5 mL of hydrazine and 3 mL of aq. NH_4NO_3 was added and the mixture was heated for 1 h at 90 °C. Hydrazine addition reduced the brownish GO to black-colored N/rGO while aqueous ammonium nitrate exfoliated the GO sheets.[33] Then, CA-N/GO(1–4) nanocomposites were prepared *via* the same ultra-sonication wet impregnation route as reported in the literature.[34] A definite amount of N/rGO was dispersed into 25 mL of water under constant stirring followed by 30 min bath ultrasonication. Then 20, 40, 60 and 80 wt% of N/rGO was poured into the CAO suspension and sonicated again for 2 hours. After that, the brownish suspension was dried for 12 hours at 80 °C, followed by sintering at 400 °C for 3 hours to evaporate the water from it. The as-obtained material was homogenized by finely grinding in a mortar and pestle and labelled as CA-N/GO1, CA-N/GO2, CA-N/GO3 and CA-N/GO4.

2.5. Photocatalytic experiment

The photocatalytic activity (PCA) of the fabricated pure CAO and CA-N/GO(1–4) nanocomposite materials were tested for the removal of crystal violet (CV) dye, which was taken as a model pollutant. A photodegradation test was conducted under visible light using a tungsten bulb of 200 watts as the light source with a UV cut-off filter. The distance between the sample mixture and the light source was adjusted to 15 cm. In the experimental procedure, 10 mg of each of the CAO and N/rGO catalysts was dissolved in 10 mg L^{-1} of CV dye solution separately. To achieve the adsorption–desorption equilibrium, the mixture was kept in the dark for 15 minutes under continuous stirring and then irradiated for 90 minutes (average intensity of 838–851.50 W m^{-2}). Approximately 3 mL aliquots were drawn out every 10 minutes, followed by centrifugation, and its absorbance value was recorded using a UV-vis spectrophotometer. The percentage removal of dye was calculated using eqn (1).

$$\text{Removal of dye } (\%) = 1 - \frac{C_t}{C_o} \times 100 \quad (1)$$

where C_o and C_t represent the absorbance values of dye solutions before and after irradiation, respectively.

3. Characterization of materials

The synthesized NMs were characterized using specific methods. The crystalline phase was analyzed *via* a Philips-X pert

PRO 3040/60 X-ray diffractometer (Cu K_α-radiation source and λ = 0.15406 nm) in a 2θ range of 20°–60°. To investigate the surface properties, SEM images were obtained using a JEOL-JSM-6490LA SEM instrument. The presence of characteristic metal–oxygen stretching and bending modes in the synthesized materials was assessed *via* Fourier transform infrared spectra obtained using a PerkinElmer Spectrum 1000-FTIR spectrometer in the 400–4000 cm^{-1} range. Magnetic hysteresis loops were obtained on a vibrating sampling magnetometer (VSM) model 7307 (Lakeshore Co.) The charge transfer ability and suppression of photo-excited electron–hole recombination in pure and composite materials were analyzed using photoluminescence emission spectra recorded using a Shimadzu RF-5301PC spectrofluorophotometer in the 300–700 nm range. The absorption behavior of all the materials was studied through their UV-vis absorption spectra in the 200–800 nm range traced using a double-beam spectrophotometer (Cary Agilent).

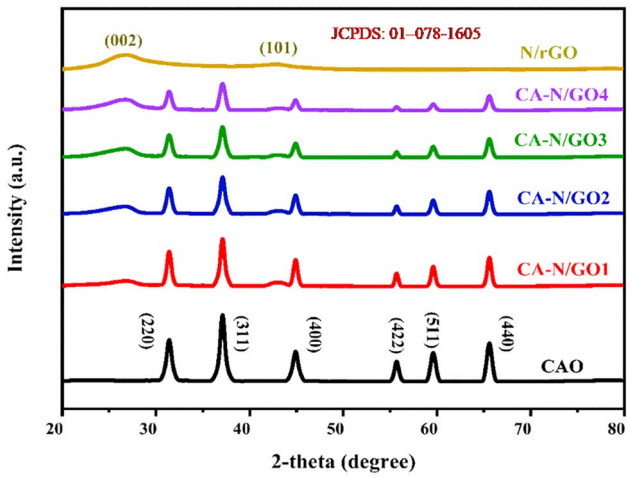

Fig. 2 XRD patterns of pure CAO, N/rGO and CA-N/GO(1–4) nanohybrids.

4. Results and discussion

4.1. Crystalline phase

Powder XRD patterns of the as-prepared pure CAO, N/rGO and CA-N/GO(1–4) materials were recorded in the 2-theta range of 20°–80° (Fig. 2). In the case of pure CAO, intense diffraction peaks were appeared around 31.25°, 36.85°, 44.74°, 55.7°, 59.37° and 65.30° that were indexed to (220), (311), (400), (422), (511) and (440) reflecting planes, respectively. All these reflections were in good agreement with JCPDS: 01-078-1605 of the cubic spinel $CuAl_2O_4$ phase and with previously reported results.[35] No secondary phase was observed for CAO in the XRD patterns, which indicated that pure cubic $CuAl_2O_4$ was formed without the formation of any other secondary phase. In the case of bare N/rGO, two diffraction peaks appeared at 26.1° and 43.21°, corresponding to the (002) and (101) crystallographic planes, respectively.[36,37]

In all the composites, the peak intensity relevant to CAO decreased while that of N/rGO increased. This observation can be ascribed to a decrease in the wt% ratio of CAO in the nanostructure. The average crystallite size of pure CAO determined using the Debye–Scherrer relation[38] was 57.32 nm.

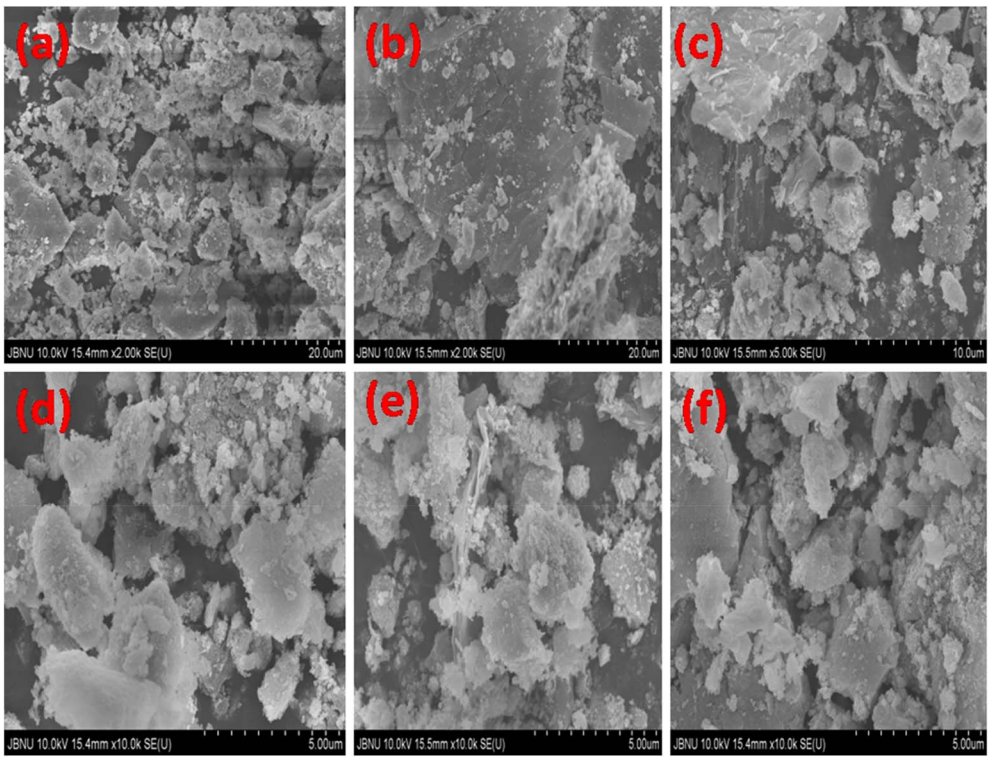

Fig. 3 SEM images of (a) CAO, (b) N-rGO and (c–f) CA-N/rGO1-4 nanohybrids.

4.2. Surface morphology

Fig. 3 shows the SEM images of pure CAO, N/rGO and CA-N/GO(1–4) heterojunctions. Results revealed that pure CAO possessed spherical nanocrystallite morphology with an average crystallite size of 61.3 nm, which is almost consistent with the XRD results. In contrast, N-rGO displayed a folding morphology with wrinkled and interconnected two-dimensional graphene sheets. The N/rGO sheets were narrowly packed and agglomerated owing to a decrease in the functional groups in GO. Moreover, these aggregations were reduced significantly in composite catalysts, possibly owing to the interaction of N-rGO with CAO, making nanohybrid catalysts favorable for strong adsorption of dye molecules on the catalyst surface.[28]

4.3. FTIR spectra

The presence of surface functional groups in the synthesized nanomaterials was studied using FTIR spectra measured in the 400–4000 cm^{-1} range. Fig. 4 shows FTIR spectra of the synthesized pure CAO, N/rGO and CA-N/GO(1–4) nanohybrids recorded at room temperature. For all the materials, broader bands appeared near 3460 and 1632 cm^{-1}. These modes can be ascribed to the –OH stretching and bending vibrational modes of the absorbed H_2O molecules present on the surface of materials.[39] In the case of pure CAO, three distinctive bands were observed at 590, 712 and 804 cm^{-1} that might be associated with stretching vibrations of Cu–O, Al–O, and Cu–O–Al bonds, respectively in pure CAO.[40,41] In the FTIR spectra of N/rGO, a broad peak was observed in the range of 3020 to 3710 cm^{-1}. This band might be ascribed to the presence of hydroxyl groups of the adsorbed water molecules on its surface.[42,43] However, the other low intensity peaks appeared at 1223, 1414 and 1717 cm^{-1} were ascribed to epoxide (C–O–C), carboxyl (COOH) and ketonic (C=O) groups, respectively.[44,45] Furthermore, the peak appeared at 1037 cm^{-1} could be attributed to C–O stretching vibrations.[46] Moreover, the N–C-related peaks in N/rGO were observed at 1608 and 1263 cm^{-1}, which were in good agreement with earlier reports.[47]

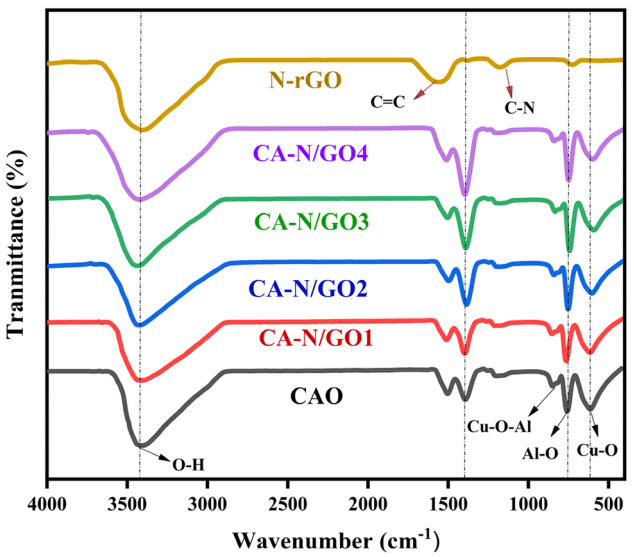

Fig. 4 FTIR spectra of pure CAO, N/rGO and CA-N/GO(1–4) nanohybrids, showing characteristic stretching and bending vibrations.

4.4. Magnetic property analysis

Fig. 5 shows the M–H loops of pure CAO, N/rGO and CA-N/GO(1–4) nanocomposites measured at 300 K. All the materials showed narrow hysteresis loops, which indicated their soft ferromagnetic nature with low saturation magnetization (M_s) values. Pure CAO demonstrated the highest value of M_s, *i.e.*, 0.027 emu g^{-1}, which was possibly due to the magnetic nature of Cu^{2+} ions in $CuAl_2O_4$.

In the N/rGO sample, a saturation magnetization of 0.0048 emu g^{-1} was observed. Although pure rGO does not show any magnetization according to previous studies, paramagnetic behavior is observed upon N doping in rGO (Table 1). This aspect can be associated to free electrons on the nitrogen atom that lead to its net magnetic moment and coercivity. For composite materials, a decreasing trend in magnetization was noticed from 0.023–0.015 emu g^{-1}. Such behavior might be attributed to the high electrical conductivity of N/rGO compared with CAO, which drops the M_s values of nanohybrids. Although CA-N/GO4 possesses the lowest M_s value, *i.e.*, 0.015 emu g^{-1}, it is still significant to be employed in magnetic applications.[48] Results reveal that the CA/NGO4 nanohybrid can be separated

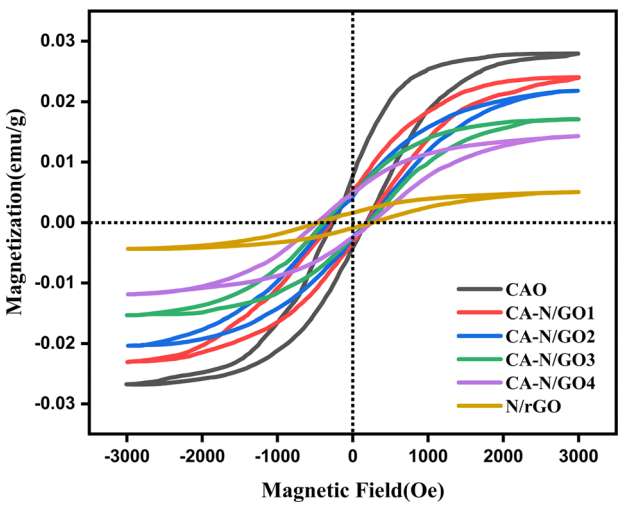

Fig. 5 M–H loops of bare CAO, N/rGO and CA-N/GO(1–4) nanohybrids.

Table 1 Magnetic parameters of bare CAO, N/rG, CA-N/rGO and composite materials

Composition	M_s (emu g^{-1})	M_r (emu g^{-1})	H_c
CAO	0.027	0.0071	286
CA/NGO1	0.023	0.0051	327
CA/NGO2	0.020	0.0049	364
CA/NGO3	0.018	0.0046	432
CA/NGO4	0.015	0.0044	527
N/rGO	0.005	0.0016	641

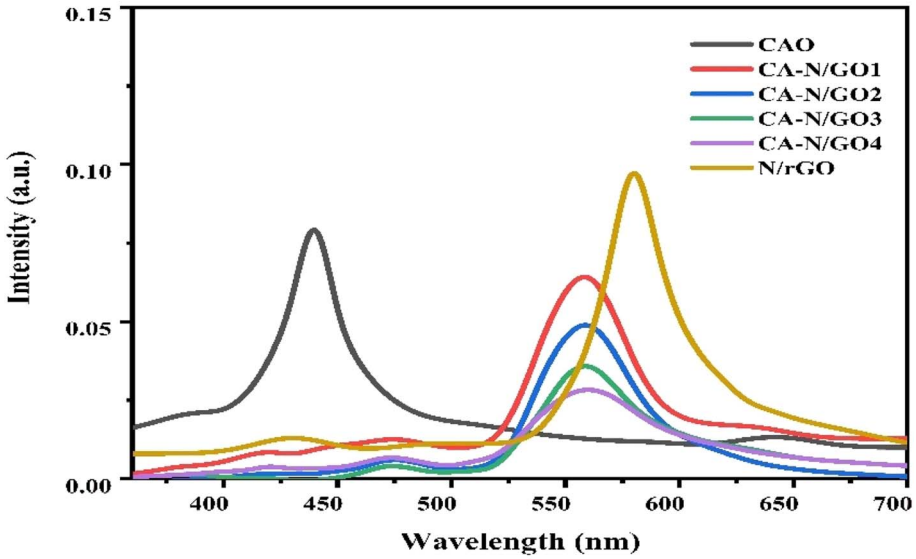

Fig. 6 PL emission spectra of pure CAO, N/rGO and CA-N/rGO nanohybrids recorded at 300 K.

easily from the reacting mixture owing to its significant magnetic moment; hence, it may find potential utilization in industrial wastewater treatment.

4.5. PL spectra

To study the recombination phenomena of the photo-induced charge carriers in pure CAO, N/rGO and heterojunction materials, the PL emission spectra were studied in the 300–700 nm range. The band gap and the relative energy positions of sub-band gap defect states can be determined from these spectra for materials intended for photocatalytic applications.[49] The recombination rate of photo-induced charge carriers was determined from the relative PL peak intensity, while their transferring rate was calculated from the PL peak height.[50] Fig. 6 depicts the PL spectra of the fabricated pure CAO, N/rGO and CA-N/GO nanocomposites recorded at 300 K. The photocatalysts showed a strong PL emission at 442 and 579 nm, indicating a rapid recombination rate of the photogenerated electrons and holes.[51] Pure CAO exhibited the highest PL intensity, followed by the CA/NGO1 composite; this intensity declined further and was at a minimum level for CA/NGO4, which possessed the highest N/rGO content in the heterojunction. This declining trend in PL intensity with increasing N/rGO levels in the nanohybrids could be explained on the basis of the introduction of new energy sub-levels within the semiconductor heterostructure that changed the transition states for the photo charges, thus inhibiting the recombination rate.[6]

4.6. UV-visible spectra

To recognize the light absorption behavior and the energy band structure of the as-prepared NPs, the UV-visible absorption spectra were obtained in the 200–800 nm absorption range

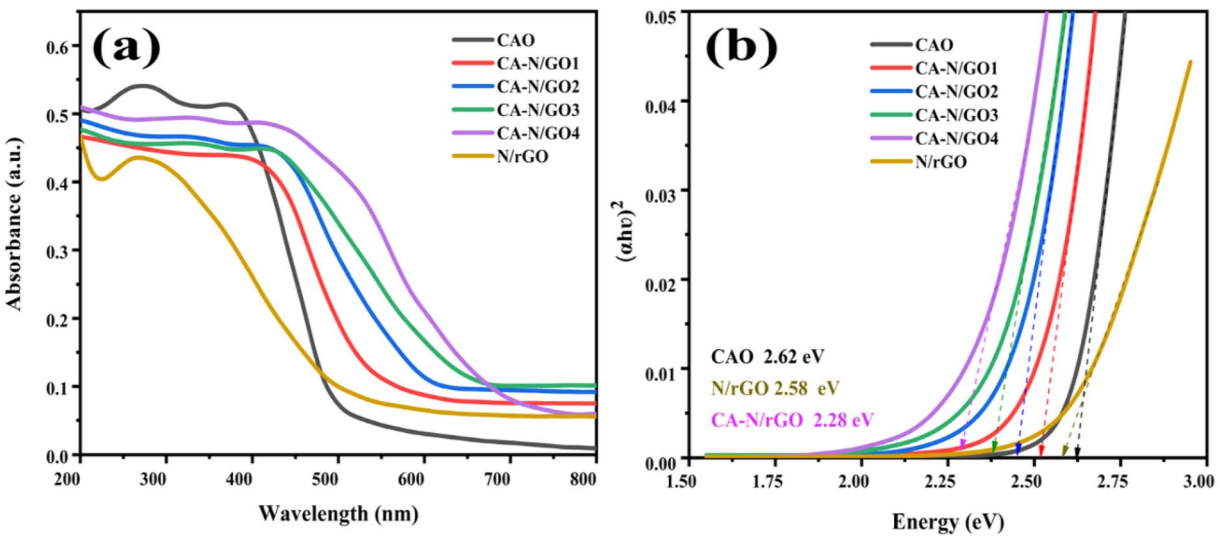

Fig. 7 (a) UV-visible absorption spectra and (b) Tauc's plot of $CuAl_2O_4$, N/rGO and CA-N/GO(1–4) nanohybrids.

(Fig. 7a). The curve shows that pure CAO has an absorption edge at about 320 nm, which indicates its activity in the UV region. The curves indicate that the absorption ability of CA-N/GO(1–4) nanohybrids was red shifted from 417 to 445 nm in the visible region when N/rGO was incorporated into CAO compared with pure CAO and N/rGO. This shift of the absorption edge can be associated with a mixing phenomenon of energy band gaps and due to the interaction between two semiconductors at the heterojunction interface that introduces defect levels in it.[52] This enhanced light absorption ability may accelerate the induction of electron–hole pairs on the composite surface which may boost its photocatalytic ability. The direct band gap energy (E_g) for the absorption spectra of CAO, N/rGO and CA-N/GO(1–4) heterostructures was estimated from Tauc plot (eqn (2)).[53]

$$(\alpha h\nu)^2 = k(h\nu - E_g)^n \quad (2)$$

where $h\nu$ is the incident photon energy in eV, while α is the absorption coefficient, E_g is the band gap energy, k is the material constant and n (=2) is a constant showing direct electronic transition. The optical band gap for pure CAO and N/rGO was calculated as 2.62 eV and 2.58 eV, respectively while for composite materials it was tuned from 2.52 to 2.28 eV (Fig. 7b). The reason for this significant drop in band gap can be associated to an improvement in the light absorption ability of the composite material. The tuned bandgap along with a sharp decline in the PL intensity synergistically improved the photocatalytic behavior of CA-N/GO(1–4) composites towards the removal of industrial dyes from polluted water.

4.7. Comparison of the photocatalytic activity

Photocatalytic activity of CA/NGO4 composite for the removal of CV dye was compared with bare CAO and N/rGO under visible-light irradiation for a 15 min time interval (Fig. 8a–c). The removal of CV dye was carried out in the presence of the above-mentioned catalysts following a 90 min exposure to visible-light irradiation.

It can be observed from the experimental results that CAO, N/rGO and CA-N/GO4 showed 48.4%, 57.1% and 82.6% removal of dye, respectively, under the same irradiation time (Fig. 9a). The enhanced catalytic efficiency of CA-N/GO4 heterostructure could be attributed to its strong light absorption, which helped in the trapping of (e^-/h^+) pairs to inhibit the recombination process. Inferior photo removal capability of CV over pure CAO and rGO could be attributed to its fast recombination of charge carriers created on their surface, resulting in a lower catalytic efficiency. Alternatively, CA-N/GO4 composites exhibited a robust catalytic performance, which can be ascribed to their strong light absorption property and ability to maintain stable e^-–h^+ pair separation for a longer period in the CA-N/GO4 heterostructure.

4.7.1. Kinetic study. To study the kinetics of MB removal over different catalysts, the Langmuir–Hinshelwood equation (eqn (3) and (4))[54] was applied:

$$C_t = C_o e^{-kt} \quad (3)$$

$$-\ln C_t/C_o = k_{app}t \quad (4)$$

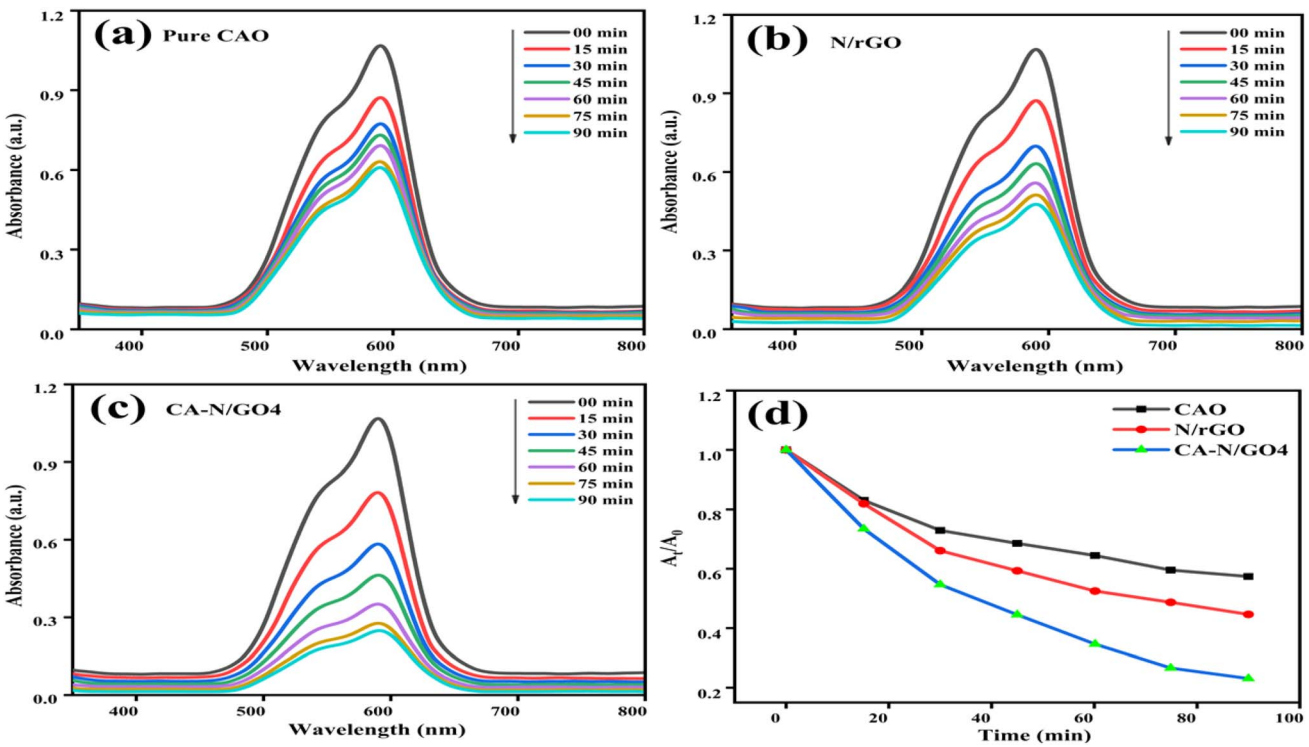

Fig. 8 (a–c) UV-visible absorption curves and (d) comparative rate of removal of CV dye over pure CAO, N/rGO and CA/rGO4 catalysts.

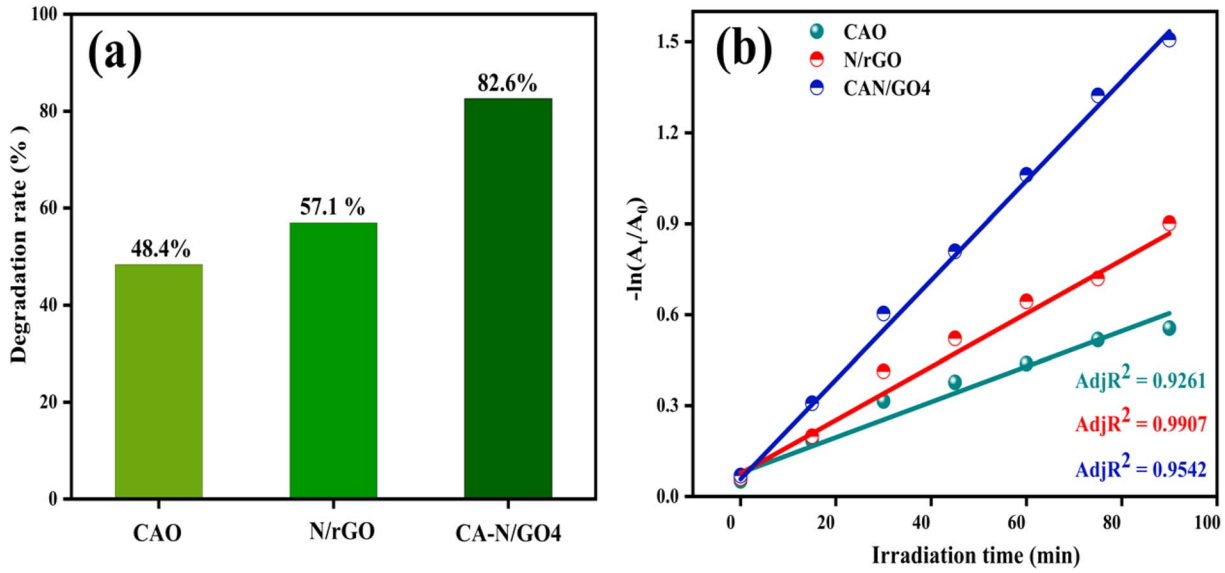

Fig. 9 (a) Percentage dye removal and (b) $-\ln A_t/A_0$ *versus* time for CAO, N/rGO and CA/GO4 for the removal of CV dye under solar irradiation.

where C_o and C_t denote the concentration of dye at zero and specific times of irradiation, respectively, while k_{app} and t are the apparent rate constant and irradiation time 't', respectively. A straight line was obtained upon plotting $-\ln A_t/A_0$ as the abscissa and irradiation time 't' as the ordinate. Linear fitting of all the plots showed that photo removal of CV follows the kinetics of pseudo-first-order over all three photocatalysts used in this work.[55] The k_{app} calculated for these catalysts was 0.019, 0.022 and 0.032 min^{-1}, respectively (Fig. 9b), where the high k_{app} value for the CA/NGO4 composite resulted in the fastest removal of dye over its surface, thus showing its superior photoactivity than the other two pure materials.

4.7.2. Influence of reaction parameters on the removal of dye

4.7.2.1 Catalyst loading. The effect of CA-N/GO4 catalyst dosage in the 10–40 mg L^{-1} range at pH 8 on photodegradation of the dye was analyzed under constant irradiation exposure time. The % dye removal efficiency increased from 82.6% to 87.3% up to 30 mg L^{-1} of the catalyst dose, but it dropped to 84.1% at 40 mg L^{-1} loading of the catalyst (Fig. 10a). This observed trend could be explained on the basis of the availability of active centers on the catalyst surface for the adsorption of dye molecules, which increases with increasing catalyst amount in the reaction mixture.[56] Furthermore, the decrease in the removal efficiency beyond 30 mg L^{-1} can be attributed to several factors, including the agglomeration of catalyst particles, suspension formation in the reaction mixture and a decrease in the irradiation penetration in aqueous medium.[57]

4.7.2.2 Effect of dye concentration. Another operational parameter which affects the removal efficiency of catalyst in aqueous medium is the concentration of dye. In this regard, the

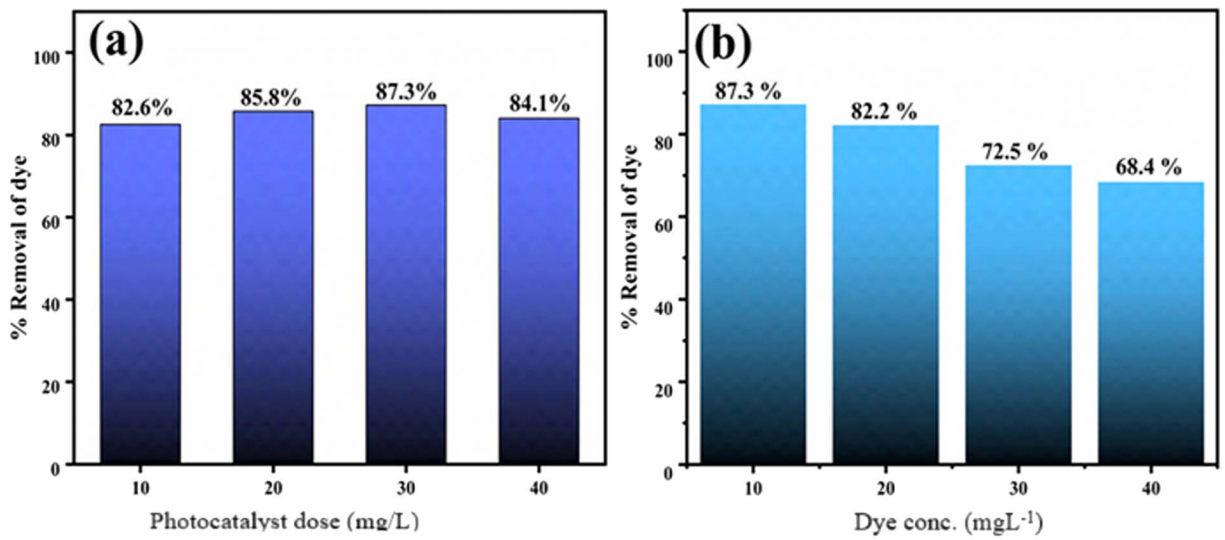

Fig. 10 (a) Effect of catalyst dose and (b) dye concentration on the removal of CV dye over CA-N/GO4 photocatalyst under solar light irradiation.

effect of the initial concentration of CV dye on its removal was studied in the 10–40 mg L^{-1} range at a constant catalyst dose of 30 mg L^{-1}. The obtained results are illustrated in Fig. 10b, which demonstrated that upon increasing the conc. of dye, the removal efficiency decreased from 87.3 to 68.4 (%). This decline in the degradation of dye could be related to the restriction in the diffusion of light in the aqueous medium of dye and an increase in the electrostatic repulsive force between dye and the photocatalyst surface.[58]

4.7.2.3 Effect of pH. Investigating the effect of pH on the rate of degradation of dyes is crucial as variation in pH significantly influences the adsorption of dye particulates on the photocatalyst surface. Therefore, understanding how the pH impacts this phenomenon is critical to optimize the degradation efficacy for effective wastewater treatment. The initial pH is one of the effective parameters in photocatalytic processes because the activity of the photocatalytic process is influenced by the surface charge of the material, molecular charge of the pollutant, adsorption of organic pollutants on the surface of the photocatalyst and the number of hydroxyl radicals in the aqueous solution.[59] Therefore, we studied the removal process of CV dye between pH 4–10, and the obtained results are shown in Fig. 11a. Maximum removal efficiency of CV dye over CA-N/GO4 catalyst was observed at pH ~10; however, above and below this pH value, the observed degradation of CV was low. This observation could be explained on the basis of zero-point charge (pH_{zpc}) on the surface of the catalyst. For CA-N/GO4 material, the pH_{zpc} was determined as 7.39, showing its surface at pH < pH_{zpc} and pH > pH_{zpc} has +ve and −ve charges, probably owing to the adsorption of protons and hydroxide ions, respectively (Fig. 11b). At pH < pH_{zpc}, both the catalyst surface and CV dye possessed positive charges, which induced an electrostatic repulsion that prevented the dye particles from arriving at the catalyst surface, thereby resulting in a lowering of its activity.[60] However, at pH > pH_{zpc}, CA-N/GO4 acquired a −ve charge on its surface, while owing to the +ve charge on CV dye, electrostatic attraction between the photocatalyst and dye increased, which ultimately increased the adsorption, and hence, the removal of dye from the reacting mixture. The as-observed results for the degradation of CV dye in basic medium were in good agreement with earlier reports.[61] By optimizing the reaction conditions, our synthesized CA-N/GO4 photocatalyst exhibited a much better activity (~99% mineralization of CV dye) under a shorter irradiation exposure time than previously used photocatalysts by various researchers (Table 2).

Table 2 Photocatalytic efficiency comparison of $CuAl_2O_4$-N/rGO photocatalyst with some previously reported materials for the removal of CV dye under visible irradiation

Photocatalyst	Light source	Time (min)	% removal	Reference
Co_3O_4 NPs	UV	45	64	62
FB-HAp	Solar	75	77	63
$ZnO/NiFe_2O_4$	Solar	140	80	64
$BaFe_{12}O_{19}$	Visible	90	91	65
ZnO/CNA	UV	120	92	66
ZnO	UV	120	96	67
ZnO-flower	UV	80	96	68
MnO_2	Visible	90	97	69
TiO_2/ZnO	UV	120	98	70
$CuAl_2O_4$-N/rGO	Visible	90	99	Present work

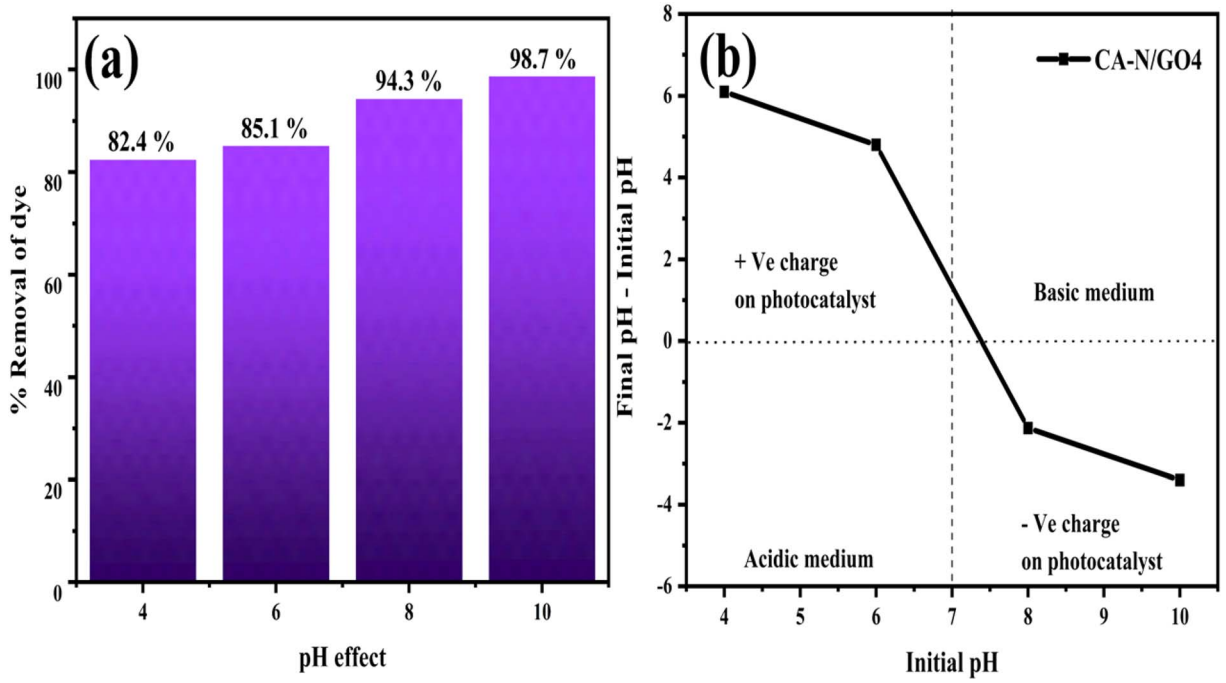

Fig. 11 (a) Effect of pH on % removal of CV dye over CA-N/GO4 photocatalyst under solar irradiation and (b) zero-point charge of CA-N/GO4.

4.7.3. Photocatalysis mechanism. To recognize the possible mechanism of removal of CV dye over CA-N/GO4 photocatalyst, active species capturing experiments were conducted by knowing the charge-transfer mechanism and identification of primary radicals responsible for the removal of CV dye. In the trapping experiment, 2-propanol, EDTA and $AgNO_3$ were applied as scavengers of $^{\bullet}OH$, h^+ and e^-, respectively. In the absence of any trapping species, the percentage removal of dye was 82.6%, whereas in the presence of the afore-mentioned agents, the % removal dropped to 31.1%, 56.5% and 45.2% with rate constants of 0.00409, 0.00871 and 0.00591 min^{-1}, respectively, as shown in Fig. 12a and b. The results showed that $^{\bullet}OH$ was the most active species in the removal of dye, while e^- also played a significant role in the degradation of dye.[71,72]

Based on the above outcomes, a probable pathway for the photodegradation of dye under solar irradiation was suggested. When a semiconducting material absorbs energy $\geq E_g$, the valence band electrons get excited to the conduction band, creating a hole there, and thus, generating an electron–hole pair on its surface, which promotes the redox process to degrade the dye absorbed on its surface.[6] It is recognized that the PCA of a semiconductor-driven photocatalyst is primarily dependent on the creation, separation and transference of photo induced electron–hole pairs. In this work, the p–n type CA-N/rGO nanocomposites played key roles in enabling the separation of these charge carriers. To completely identify the construction of this heterojunction, the valence and conduction band positions of N/rGO and CAO were calculated using empirical relations shown in eqn (5) and (6):[73]

$$E_{VB} = \chi - E_e + 0.5E_g \quad (5)$$

$$E_{CB} = E_{VB} - E_g \quad (6)$$

where E_{VB} and E_{CB} are the valence and conduction band potentials, respectively, E_e is the energy of free electrons on the hydrogen scale (~4.5 eV), while χ is the absolute electronegativity (geometric mean of the absolute electronegativity of the constituent atoms) of the semiconductor and is defined as the arithmetic mean of electron affinity and first ionization potential.[74] From the χ values of pure CAO and N/rGO, their valence band potentials were calculated as 1.5 and 2.65 V *vs.* NHE, respectively.

Enhanced photocatalytic activity of the CA-N/GO4 nanohybrid was associated with its band structure. In the heterojunction structure, the direction of electron flow depends on corresponding band-edge positions. Hence, a probable mechanism for the better electron transport in the heterojunction photocatalyst was postulated. As the CB level of N/rGO is less than CAO, the electrons in CB of CAO are possibly shifted to that of N/rGO under solar irradiation. As the VB level of N/rGO is lower than that of CAO, holes (h^+) in its VB was shifted towards the VB of CAO (Fig. 13).

Ultimately, the separation and migration of photo-induced charge carriers can be facilitated by the internal field where a lower barrier starts to exist. In this way, the probability of recombination of the electron–hole can be reduced to a great extent as a large number of active electrons and holes on the N/rGO and CAO surface in the CA-N/GO4 heterostructure can participate in photo-driven redox reaction of dye.[6,28] The above outcomes can be correlated with the PL results, where separation and rejoining of photo-induced charges are directly dependent on PL peak intensity. For composite materials, the PL signal becomes significantly weaker after formation of the heterostructure with N/rGO; this determines the remarkable restriction of the recombination of charge carriers. Active electrons on CB of N/rGO can be trapped by molecular O_2 adsorbed on its surface to form superoxide radical anion *i.e.*, $O_2^{\bullet -}$, which is ultimately converted into hydroxyl $OH^{\bullet}$ radicals through several reactions. These radicals can directly remove dye from the reacting mixture under irradiation. Besides, reactive holes on the VB of CAO may oxidize the organic dye owing to its strong oxidizing power, as shown below in the chemical reactions below.

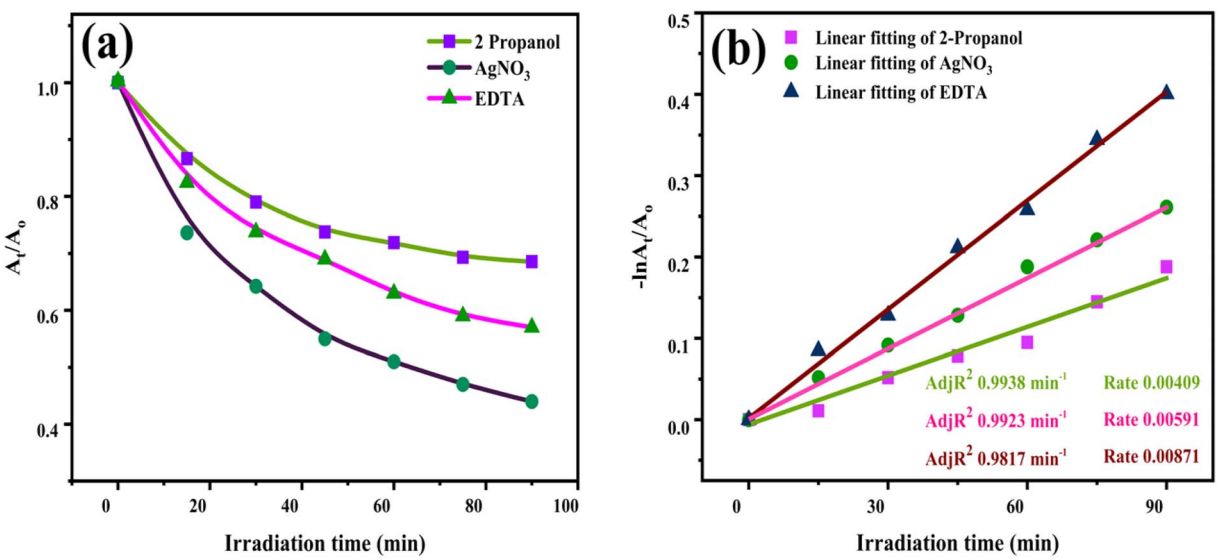

Fig. 12 A_t/A_0 curves (a) and (b) rate constant of scavengers for the removal of CV dye over CA-N/GO4 catalyst.

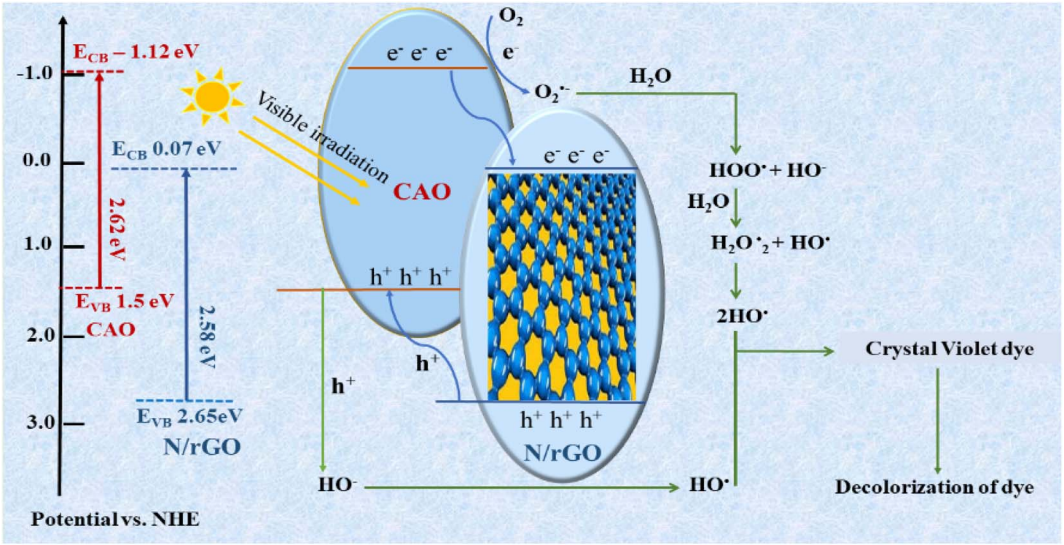

Fig. 13 Schematic of the probable pathway for photocatalytic removal of CV dye over CA-N/GO4 catalyst under solar irradiation.

$$\text{CA-N/GO4} + \text{irradiation} \rightarrow (e^-)_{(CB)} + (h^+)_{(VB)}$$

$$e^- + O_2 \rightarrow O_2^{\bullet -}$$

$$h^+ + H_2O/OH^- \rightarrow {}^{\bullet}OH$$

$$O_2^{\bullet -} + H_2O \rightarrow {}^{\bullet}OOH + OH^- \rightarrow H_2O_2$$

$$H_2O_2 + O_2^{\bullet -} \rightarrow {}^{\bullet}OH + OH$$

$$\text{CV dye} + {}^{\bullet}OH + O_2^{\bullet -} \rightarrow H_2O + CO_2 + \text{inorganic ions}$$

4.7.4. Reusability and structural stability. Reusability and structural stability of CA-N/GO4 photocatalyst for practical applications were evaluated for four consecutive cyclic runs under a constant exposure time. Used CA-N/GO4 NPs were recollected from aqueous medium through an applied magnetic field and were dried at 70 °C. Results showed that the % removal of dye for the 2nd, 3rd and 4th cycle dropped to 96.5, 91.7, and 89.3 (%), respectively (Fig. 14). This loss in removal efficiency could be attributed to a reduction in the active surface area, which was due to a loss in mass at the end of each run.[75] These outcomes indicated that CA-N/GO4 nanocomposites exhibited good recoverability with fair stability, finding its practical implication in efficient removal of dye from industrial effluents.

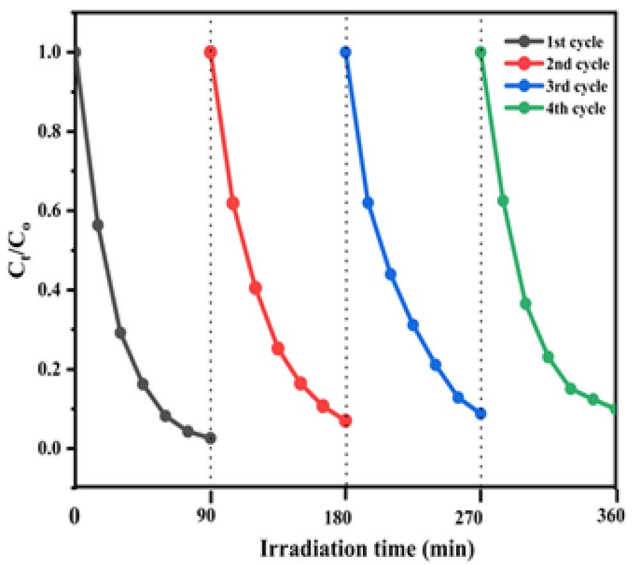

Fig. 14 C_t/C_o *versus* time curves for the removal of CV dye over CA-N/GO4 for various cycles.

5. Conclusions

This study investigated the effect of N/rGO on the photocatalytic activity of CA-N/rGO nanohybrids for the photocatalytic removal of crystal violet dye under visible light. Diffraction patterns showed the characteristic peaks of cubic spinal $CuAl_2O_4$ and N/rGO in CA-N/GO4 heterojunction. Furthermore, the corresponding metal–oxygen functional groups in CAO were retained in all the composites, as evidenced by the FTIR spectra. The presence of N/rGO in the heterojunction resulted in an increase in the visible light absorption and it narrowed the bandgap that led to an enhanced photocatalytic efficiency. Specifically, the bandgap was tuned from 2.52 eV to 2.28 eV with an increase in the N/rGO content. PL measurements revealed that CA-N/GO4 material exhibited the lowest emission intensity compared with pure CAO, suggesting its lower recombination rate of photo-induced electron–hole pairs on the interface. The CA-N/GO4 nanohybrid revealed superior degradation efficiency by showing 82.6% removal of dye, while the pure $CuAl_2O_4$ and N/rGO only showed 48.4% and 57.1% degradation of the dye, respectively. Moreover, the rate of photodegradation of the dye improved from 0.019 min^{-1} (CAO) and 0.022 min^{-1} (N/rGO) to 0.032 min^{-1} for CA-N/GO4 at pH 7 using 10 mg L^{-1} of dye. Upon

incorporation of N/rGO into CA-N/GO4, saturation magnetization significantly decreased from 0.027 to 0.015 emu g^{-1}, which was still enough to recover it from the reaction mixture at the end of the process. The catalytic activity of CA-N/GO4 was still preserved with a minor decline of 9.4% even after four successive cyclic runs for CV dye removal. Scavenging results showed that $^{\bullet}OH$ and e^{-} were the main active species in the removal of dye over the CA-N/GO4 heterojunction. Thus, the novel CA-N/GO4 nanohybrid with the synergistic effects of superior catalytic activity and robust magnetic reparability has potential applicability in the removal of dyes from discharged water of dying units under visible irradiation.

Data availability

The data used to support the findings of this study are available from the corresponding author upon request.

Conflicts of interest

There are no conflicts to declare.

Acknowledgements

The authors express their gratitude to Princess Nourah bint Abdulrahman University Researchers Supporting Project number (PNURSP2025R11), Princess Nourah bint Abdulrahman University, Riyadh, Saudi Arabia.

References

1 Y. Jia and K. Zhang, *RSC Adv.*, 2025, **15**, 8764–8776.
2 H. H. Aya, N. Djamel, A. Samira, M. Otero and M. A. Khan, *RSC Adv.s*, 2024, **14**, 23816–23827.
3 M. Iqbal, M. Abbas, A. Nazir and A. Z. Qamar, *Chem. Int.*, 2019, **5**, 1–80.
4 S. Kokilavani, A. Syed, A. M. Thomas, A. M. Elgorban, S. Al-Rashed, L. L. Raju and S. S. Khan, *J. Alloys Compd.*, 2021, **865**, 158810.
5 A. Chinnathambi, O. Nasif, S. A. Alharbi and S. S. Khan, *Mater. Sci. Semicond. Process.*, 2021, **134**, 105992.
6 V. V. Sre, M. K. Okla, B. Janani, M. A. Abdel-Maksoud, S. S. Al-Amri, I. A. Alaraidh, A. A. Alatar and S. S. Khan, *J. Water Process Eng.*, 2024, **59**, 104957.
7 G. Ren, Q. Ren, Z. Ren, P. Chen, M. Yue, N. Sun, J. Gao, J. Wu, Y. Fu and J. Ma, *Opt. Express*, 2025, **33**, 13682–13694.
8 J. P. Steffy, A. Syed, C. Kamaraj, S. Naveenkumar, A. M. Thomas, A. M. Elgorban, I. Abid, L. L. Raju, L. S. Wong and S. S. Khan, *Sustainable Mater. Technol.*, 2025, **43**, e01185.
9 A. Yousefinia, M. Khodadadi and S. Mortazavi-Derazkola, *Environ. Technol. Innovation*, 2023, **32**, 103340.
10 Z. Kiani, S. Mirjalili, K. Heydaryan, P. Mohammadparast, H. Aramjoo, F. Bahraini, A. Yousefinia, M. Torabi, S. M. Ghoreishi, M. Fattahi and S. Mortazavi-Derazkola, *J. Drug Delivery Sci. Technol.*, 2024, **96**, 105708.
11 S. Mohammadi-Aghdam, F. Bahraini and S. M. Ghoreishi, *Biomass Convers. Biorefin.*, 2024, **14**, 20037–20052.
12 K. Khormali, Z. M. Mizwari, S. Masoumeh Ghoreishi, S. Mortazavi-Derazkola and B. Khezri, *Bioorg. Chem.*, 2021, **115**, 105204.
13 J. Guo, Y. Li, S. Li, X. Cui, Y. Liu, W. Huang, L. Mao, X. Wei and X. Zhang, *Chin. J. Catal.*, 2020, **41**, 1208–1216.
14 K.-L. Zhang, C.-M. Liu, F.-Q. Huang, C. Zheng and W.-D. Wang, *Appl. Catal., B*, 2006, **68**, 125–129.
15 M. Shirzadi-Ahodashti, M. A. Ebrahimzadeh, S. M. Ghoreishi, A. Naghizadeh and S. Mortazavi-Derazkola, *Appl. Organomet. Chem.*, 2020, **34**, e5614.
16 S. M. Ghoreishi, *J. Mater. Sci.: Mater. Electron.*, 2017, **28**, 14833–14838.
17 F.-P. Huang, W.-J. Qin, X.-Y. Pan, K. Yang, K. Wang and Q.-H. Teng, *J. Org. Chem.*, 2024, **89**, 4395–4405.
18 P. Chandran, S. Netha and S. Sudheer Khan, *J. Photochem. Photobiol., B*, 2014, **138**, 155–159.
19 M. B. Safa, J. P. Steffy, A. T. Alfagham, A. M. Elgorban and S. S. Khan, *J. Water Process Eng.*, 2025, **71**, 107113.
20 S. M. Ghoreishi and S. Mortazavi-Derazkola, *Heliyon*, 2025, **11**, e40104.
21 Q. Tian, M. Ran, G. Fang, L. Ding, A. Pan, K. Shen and Y. Deng, *Sep. Purif. Technol.*, 2020, **239**, 116574.
22 S. Hassanzadeh-Tabrizi, R. Pournajaf, A. Moradi-Faradonbeh and S. Sadeghinejad, *Ceram. Int.*, 2016, **42**, 14121–14125.
23 Y. Behnamian, E. Aghaie, D. Serate, Z. Tolentino, H. Niazi and A. Mostafaei, *Ceram. Int.*, 2022, **48**, 27988–27994.
24 W. Chen, J. Huang, Z.-C. He, X. Ji, Y.-F. Zhang, H.-L. Sun, K. Wang and Z.-W. Su, *Sep. Purif. Technol.*, 2021, **277**, 119461.
25 W. Lv, B. Liu, Q. Qiu, F. Wang, Z. Luo, P. Zhang and S. Wei, *J. Alloys Compd.*, 2009, **479**, 480–483.
26 B. Mandal, J. Panda, P. K. Paul, R. Sarkar and B. Tudu, *Vacuum*, 2020, **173**, 109150.
27 J. Zhang, J. Xin, C. Shao, X. Li, X. Li, S. Liu and Y. Liu, *J. Colloid Interface Sci.*, 2019, **550**, 170–179.
28 L. Sruthi, M. K. Okla, B. Janani, M. A. Abdel-Maksoud, I. A. Saleh, H. A. Abu-Harirah and S. S. Khan, *J. Cleaner Prod.*, 2024, **434**, 139936.
29 S. Firdous, I. Bibi, F. Majid, H. Elhouichet, A. Ghafoor, Q. Raza, G. Fatima, A. B. G. Trabelsi, F. H. Alkallas and M. Iqbal, *Sol. Energy*, 2024, **274**, 112540.
30 N. Chnadel, V. Dutta, S. Sharma, P. Raizada, A. Hosseini-Bandegharaei, R. Kumar, P. Singh and V. Thakur, *Mater. Today Sustain.*, 2020, **9**, 100043.
31 S. Padhiari, M. Tripathy and G. Hota, *ACS Appl. Nano Mater.*, 2021, **4**, 7145–7161.
32 S. Iqbal, I. Bibi, S. Ata, S. Kamal, S. M. Ibrahim and M. Iqbal, *Diamond Relat. Mater.*, 2020, **110**, 108119.
33 A. Rahman, M. Aadil, M. Akhtar, M. F. Warsi, A. Jamil, I. Shakir and M. Shahid, *Ceram. Int.*, 2020, **46**, 13517–13526.
34 H. Y. Hafeez, S. K. Lakhera, P. Karthik, M. Anpo and B. Neppolian, *Appl. Surf. Sci.*, 2018, **449**, 772–779.
35 M. Kaci, N. Nasrallah, F. Atmani, M. Kebir, R. Guernanou, A. Soukeur and M. Trari, *Res. Chem. Intermed.*, 2021, **47**, 3785–3806.

36 F. A. Alharthi, A. S. Ababtain, H. K. Aldubeikl, H. S. Alanazi and I. Hasan, *Inorganics*, 2023, **11**, 67.
37 S. R. Chandrabhan, V. Jayan, S. S. Parihar and S. Ramaprabhu, *Beilstein J. Nanotechnol.*, 2017, **8**, 1476–1483.
38 G. Lincke, *Dyes Pigm.*, 2000, **44**, 101–122.
39 D.-L. Ge, Y.-J. Fan, C.-L. Qi and Z.-X. Sun, *J. Mater. Chem. A*, 2013, **1**, 1651–1658.
40 W. Lv, Z. Luo, H. Yang, B. Liu, W. Weng and J. Liu, *Ultrason. Sonochem.*, 2010, **17**, 344–351.
41 M. Salavati-Niasari, F. Davar and M. Farhadi, *J. Sol-Gel Sci. Technol.*, 2009, **51**, 48–52.
42 A. C. Ferrari, *Solid State Commun.*, 2007, **143**, 47–57.
43 C. Hontoria-Lucas, A. López-Peinado, J. d. D. López-González, M. Rojas-Cervantes and R. Martín-Aranda, *Carbon*, 1995, **33**, 1585–1592.
44 M. Acik, G. Lee, C. Mattevi, A. Pirkle, R. M. Wallace, M. Chhowalla, K. Cho and Y. Chabal, *J. Phys. Chem. C*, 2011, **115**, 19761–19781.
45 A. J. Page, C.-P. Chou, B. Q. Pham, H. A. Witek, S. Irle and K. Morokuma, *Phys. Chem. Chem. Phys.*, 2013, **15**, 3725–3735.
46 A. K. Das, M. Srivastav, R. K. Layek, M. E. Uddin, D. Jung, N. H. Kim and J. H. Lee, *J. Mater. Chem. A*, 2014, **2**, 1332–1340.
47 G. Witjaksono, M. Junaid, M. H. Khir, Z. Ullah, N. Tansu, M. S. B. M. Saheed, M. A. Siddiqui, S. S. Ba-Hashwan, A. S. Algamili and S. A. Magsi, *Molecules*, 2021, **26**, 6424.
48 T. Govindasamy, M. Nandhakumar, N. K. Mathew, R. V. Kulangara, V. K. Asapu, S. Padmanapan, D. T. Thangaian and B. Subramanian, *J. Mater. Res.*, 2022, **37**, 1216–1230.
49 T. Tangcharoen, J. T-Thienprasert and C. Kongmark, *J. Adv. Ceram.*, 2019, **8**, 352–366.
50 M. Mao, J. Xu, L. Li, S. Zhao, X. Li, Y. Li and Z. Liu, *Ionics*, 2019, **25**, 4533–4546.
51 K. Saravanan and P. SivaKarthik, *J. Cluster Sci.*, 2020, **31**, 401–407.
52 P. Hankare, R. Patil, A. Jadhav, K. Garadkar and R. Sasikala, *Appl. Catal., B*, 2011, **107**, 333–339.
53 P. Makuła, M. Pacia and W. Macyk, *J. Phys. Chem. Lett.*, 2018, **9**, 6814–6817.
54 T. Soltani and M. H. Entezari, *Chem. Eng. J.*, 2013, **223**, 145–154.
55 J.-P. Simonin, *Chem. Eng. J.*, 2016, **300**, 254–263.
56 G. Eshaq and A. E. ElMetwally, *Ultrason. Sonochem.*, 2019, **53**, 99–109.
57 N. Belhouchet, B. Hamdi, H. Chenchouni and Y. Bessekhouad, *J. Photochem. Photobiol., A*, 2019, **372**, 196–205.
58 L. Ghalamchi and S. Aber, *Mater. Chem. Phys.*, 2020, **256**, 123649.
59 A. El-Bindary, A. Ismail and E. Eladl, *J. Mater. Environ. Sci.*, 2019, **10**, 1258–1271.
60 M. S. Nas, *J. Environ. Chem. Eng.*, 2021, **9**, 105207.
61 F. Mejbar, Y. Miyah, A. Lahrichi, S. Ssouni, A. Khalil, L. Nahali, M. Benjelloun, G. El Mouhri and F. Zerrouq, *Moroccan J. Chem.*, 2021, **9**(9–3), 2434–2445.
62 R. S. Saravan, M. Muthukumaran, S. Mubashera, M. Abinaya, P. V. Prasath, R. Parthiban, F. Mohammad, W. C. Oh and S. Sagadevan, *Optik*, 2020, **207**, 164428.
63 S. Sathiyavimal, S. Vasantharaj, M. Shanmugavel, E. Manikandan, P. Nguyen-Tri, K. Brindhadevi and A. Pugazhendhi, *Prog. Org. Coat.*, 2020, **148**, 105890.
64 A. Ihsan, A. Irshad, M. F. Warsi, M. I. Din and S. Zulfiqar, *Opt. Mater.*, 2022, **134**, 113213.
65 Misbah, I. Bibi, F. Majid, S. Kamal, K. Jilani, B. Taj, Z. Nazeer and M. Iqbal, *J. Saudi Chem. Soc.*, 2022, **26**, 101533.
66 Z. A. Messaoudi, D. Lahcene, T. Benaissa, M. Messaoudi, B. Zahraoui, M. Belhachemi and A. Choukchou-Braham, *Chem. Methodol.*, 2022, **6**, 661–676.
67 M. Assassi, F. Madjene, S. Harchouche and H. Boulfiza, *Environ. Prog. Sustainable Energy*, 2021, **40**, e13702.
68 S. Ameen, M. S. Akhtar, M. Nazim and H.-S. Shin, *Mater. Lett.*, 2013, **96**, 228–232.
69 M. Rahmat, A. Rehman, S. Rahmat, H. N. Bhatti, M. Iqbal, W. S. Khan, S. Z. Bajwa, R. Rahmat and A. Nazir, *J. Mater. Res. Technol.*, 2019, **8**, 5149–5159.
70 M. Sifat, E. Shin, A. Schevon, H. Ramos, A. Pophali, H.-J. Jung, G. Halada, Y. Meng, N. Olynik and D. J. Sprouster, *Catalysts*, 2024, **14**, 377.
71 N. M. Hussein and S. Mortazavi-Derazkola, *J. Alloys Compd.*, 2025, **1022**, 179987.
72 N. M. Hussein and S. Mortazavi-Derazkola, *Colloids Surf., A*, 2025, **714**, 136585.
73 T. Xian, H. Yang, L. Di and J. Dai, *J. Alloys Compd.*, 2015, **622**, 1098–1104.
74 H. Zhang, Y. Yang, Z. Zhou, Y. Zhao and L. Liu, *J. Phys. Chem. C*, 2014, **118**, 14662–14669.
75 A. Samal, S. Swain, B. Satpati, D. P. Das and B. K. Mishra, *ChemSusChem*, 2016, **9**, 3150–3160.